https://doi.org/10.1016/j.nanoen.2021.106251

Tunable One-Dimensional Inorganic Perovskite Nanomeshes Library for Water Splitting

Yecan Pi,[1,2] Qi Shao,[2] Juan Wang,[2] Bolong Huang,[3,4] Zhiwei Hu[5] Chien-Te Chen,[6] Chih-Wen Pao,[6] Xiangfeng Duan,[7] and Xiaoqing Huang[1,*]*

[1]State Key Laboratory of Physical Chemistry of Solid Surfaces, College of Chemistry and Chemical Engineering, Xiamen University, Xiamen 361005, China.
[2]College of Chemistry, Chemical Engineering and Materials Science, Soochow University, Suzhou, Jiangsu 215123, China.
[3]Department of Applied Biology and Chemical Technology, The Hong Kong Polytechnic University, Hung Hom, Kowloon, Hong Kong SAR, China.
[4]Beijing Institute of Nanoenergy and Nanosystems, Chinese Academy of Sciences, Beijing, China
[5]Max-Planck-Institute for Chemical Physics of Solids, Nöthnitzer Street 40, Dresden 01187, Germany.
[6]National Synchrotron Radiation Research Center, 101 Hsin-Ann Road, Hsinchu 30076, Taiwan.
[7]Department of Chemistry and Biochemistry, University of California, Los Angeles, CA 90095, USA.
*Email: bhuang@polyu.edu.hk (B.H.), hxq006@xmu.edu.cn (X.H.).

Keywords: Perovskite, One-dimensional structure library, Nanomesh, Electrocatalysis, Water splitting

Abstract

Perovskites are highly promising candidates in future energy conversion and storage due to their rich diversities and readily tunable electronic properties. However, the poor morphology controllability and limited surface areas have severely limited their applications. We present a generalizable synthesis strategy to fabricate a library of one-dimensional (1D) inorganic perovskite nanomeshes via pyrolysis of metal salt-polymer fibers. Within the evaluated perovskite nanomeshes, $La_{0.5}Ba_{0.5}Co_{0.8}Ni_{0.2}O_3$ delivers the most remarkable performance for the oxygen evolution reaction (OER). Combined X-ray absorption spectroscopy experiments and density functional theory calculations reveal that introduction of additional metals endows more flexible electronic structures to realize the electron transfer in 1D perovskite nanomeshes. This work demonstrates a scalable and retrosynthetic route to easily synthesize the inorganic perovskite nanomaterials with tunable composition.

Introduction

Advances in energy conversion and storage systems are essential for exploring renewable energy to address the rapidly growing energy demands and environmental issues.[1,2] Electrocatalysts play a crucial role in many sustainable energy technologies such as fuel cells, rechargeable metal-air batteries, water splitting and carbon dioxide/nitrogen reduction, to increase the rate, efficiency, and selectivity of the chemical transformations involved.[3-7] Currently, platinum group metals (PGM) (*e.g.*, Pt, Pd, Ir and Ru) represent the most efficient and commonly used electrocatalysts, but their high cost and scarcity greatly impede their practical applications and widespread adoption of the relevant technologies.[8-14] Therefore, developing efficient and cost-effective PGM-free alternatives is of great significance to meet the global energy and environmental needs.

In the past decades, perovskite oxides (ABO_3, where A are alkaline-earth or rare-earth metals and B are transition metals) have attracted great interest for their flexible compositions and crystal structures, which endows the highly tunable electronic properties that can be used for realizing active, selective, and stable catalysis.[15,16] To date, multiple theories (*e.g.*, bulk formation energy, e_g occupancy, outer electrons, ionic electronegativity, oxidation state and multi-physicochemical material properties, *etc.*) have been proposed to elucidate the principles between parameter and intrinsic activity of perovskites, which give rational guidance toward the development of improved electrocatalysts for targeting electrocatalysis, such as oxygen reduction reaction (ORR), oxygen and hydrogen evolution reactions (OER and HER).[17-21] Despite these significant efforts, the perovskite electrocatalysts still suffer from poor practical performances. For example, the most reported perovskites for OER usually required overpotential > 350 mV to achieve the current density of 10 mA cm^{-2}, which is still much inferior to the precious metal catalysts (Table S1). A key reason is the poor morphology control of conventional synthesis methods under extra-high calcination temperature, which usually results in irregular particle shape with low specific surface area.[22-25] Generally, tailoring the geometrical factors including creating smaller size or porous nanostructures will help to expose more accessible active sites and result in a ready promotion on catalysis.[5, 26-30] In addition, compared to the assembly of individual discrete particles, it is believed that the cross-linked network feature of one-dimensional (1D) structure is favorable for the diffusion of reactants and electrical transport, and simultaneously more resistant to agglomeration and Oswald ripening, enabling enhancement in both activity and durability.[31-36]

Herein, we report a general route to produce highly porous 1D inorganic perovskite nanomeshes by the pyrolysis of metal salt-polymer fibers. Using this approach, we have successfully obtained various multielement perovskites with up to six dissimilar metal elements. The created perovskites have a high-quality 1D structure with densely dispersed pores. By combining the advantages of flexible compositions, porous structure with high specific surface area, and cross-linked network structure, advanced perovskite electrocatalyst with exceptional performance is expected. As a proof of concept, we evaluate the OER performance of a series of Co-based 1D perovskite nanomeshes, in which the $La_{0.5}Ba_{0.5}Co_{0.8}Ni_{0.2}O_3$ (LBCNO) exhibits an outstanding activity that can achieve a current density of 100 mA cm^{-2} at an overpotential of only 364 mV, and superior stability at large current densities (50 mA cm^{-2}) for at least 30 h, which already exceeds the state-of-the-art commercial RuO_2. X-ray absorption spectroscopy (XAS) analysis combined theoretical calculations indicate that the introduction of Ba and Ni results in the lower oxidation state and regulated spin state of Co, associating with the compressed Co-O bond in LBCNO nanomesh, which has contributed to the intermediate adsorption and the electron transfer in the OER catalysis.

Results and Discussion

An illustration of the route to create 1D perovskite nanomeshes is shown in **Figure 1a**. In a typical procedure, the metal nitrates and polymer (polyvinyl pyrrolidone, PVP) were mixed in a certain proportion and dissolved in N, N-dimethylformamide (DMF), to form a uniform viscous solution. The resulting solution was then loaded into a plastic syringe equipped with a thin nozzle. During the electrospinning process, a high voltage (~16 kV) is applied between the nozzle and collector, which induces a charge on the surface of the polymer solution. Once the strength of the electric field is high enough to allow the repulsive electrostatic force to overcome the surface tension of the polymer solution, a liquid jet (known as the Taylor cone) forms and moves towards the collector.[37,38] Before reaching the collector, the discharged polymer solution jet undergoes an instability and elongation process to become longer and thinner. Meanwhile, the solvent evaporates gradually, and solid fibers are finally precipitated on the collector. Using this approach, various metal precursors can be evenly (ideally at the atomic level) dispersed in the prepared polymer fibers, which makes a unique start for the formation of perovskites. Subsequently, the metal salt-polymer fiber is calcined at 600 ~ 700 ºC under air to generate phase-pure perovskite oxides. During this process, a large quantity of gaseous products is produced, which is the key to the formation of the porous 1D mesh-like structure.

Taking 1D $LaCoO_3$ (LCO) perovskite nanomesh as a representative example. $La(NO_3)_3 \cdot 6H_2O$ (1 mmol) and $Co(NO_3)_2 \cdot 6H_2O$ (1 mmol) were dispersed in a PVP/DMF solution (14 wt.% based on the mass of DMF) to form a precursor solution for electrospinning. The obtained pristine metal salt-polymer fibers have high-quality 1D morphology and smooth surface, with a diameter of about 200~400 nm and a length of dozens of microns (**Figure S1a,b**). The pristine metal salt-polymer fibers were then calcined at 600 ºC for 3 h in air atmosphere to generate the 1D perovskite nanomesh (**Figure S1c,d**). Significantly, the proposed synthetic strategy is robust, which is able to fabricate the 1D perovskite nanomeshes library by readily introducing desired metal nitrates at the beginning of the synthetic procedure. **Figure 1b-f** and **Figures S2-S20** show the detailed characterizations for the 1D perovskite nanomeshes library. We synthesized binary (La-Mn, La-Fe, La-Ni, Pr-Mn, Pr-Fe, Pr-Co) 1D perovskite nanomeshes, which have similar structural features with 1D LCO nanomeshes, as revealed by the SEM and HAADF-STEM images (**Figure 1b**). Elemental mappings show the homogeneous spatial distributions of metal elements and oxygen in 1D nanomeshes. Their perovskite phases were confirmed by XRD. Moreover, we have further successfully synthesized a series of ternary (La-Pr-Co, La-Ba-Co, La-Y-Co, La-Co-Mn, La-Co-Fe and La-Co-Ni) 1D perovskite nanomeshes (**Figure 1c**). In all cases, the high quality of 1D nanostructures can be well maintained, and the unique dense porosity is also observed. Beyond the common binary and ternary structure, we have innovatively extended the library to much more complicated quaternary (La-Pr-Co-Fe, Pr-Y-Co-Mn and La-Ba-Co-Ni), quinary (La-Pr-Co-Ni-Mn, La-Pr-Ba-Co-Fe) and even senary (La-Pr-Ba-Co-Ni-Fe) 1D perovskite nanomeshes (**Figure 1d-f**). As confirmed by SEM, elemental mappings and XRD, clearly showing the versatility of the synthesis reported herein.

As shown in **Figure 2a**, the synthesized 1D LCO perovskite nanomeshes maintain the uniform 1D morphology without aggregation and fracture. More interestingly, there are dense pores distributed across the 1D structure, forming a highly porous mesh-like feature that is connected to the small crystalline grains, as revealed by the magnified HAADF-STEM images (**Figure 2b** and **Figure S21a,b**). The selected-area electron-diffraction (SAED) pattern of an individual 1D nanomesh reveals its polycrystalline feature (**Figure 2c**). The crystal phase of obtained nanomesh was further confirmed by X-ray diffraction (XRD) pattern, in which all the diffraction peaks could be indexed to LCO perovskite (JCPDS number 75-0279) with no signal of possible crystalline impurities detected, suggesting its pure perovskite phase (**Figure 2d**). High-resolution TEM (HRTEM) image shows lattice fringes with the interplanar spacing of 0.38 nm and 0.22 nm, which can correspond to the (100) and (111) planes of perovskite-type lanthanum cobaltite, respectively (**Figure 2e**). Energy-dispersive X-ray spectroscopy (EDS) analysis demonstrates that La (green), Co (blue), and O (red) are distributed uniformly at the nanomesh (**Figure 2f** and **Figure S21c**). Therefore, by combining the metal salt-polymer fiber and pyrolysis strategy, we have successfully created highly porous 1D LCO perovskite nanomeshes. Naturally, such obtained perovskite nanomesh holds a high specific area (13.4 m^2 g^{-1}) (**Figure S21d**), which is one order of magnitude higher than most reported perovskites made by conventional methods.[39-41] Moreover, lots of edge sites in such unique nanostructure can also provide numerous coordinatively unsaturated atoms, which would be favorable for advanced electrocatalysis.[27,42,43]

To gain an in-depth understanding of the formation mechanism of the 1D perovskite nanomesh, thermogravimetric analysis (TGA) measurements were carried out to investigate the evolution during the calcination process. As shown in **Figure S22**, $La(NO_3)_3{\cdot}6H_2O$ and $Co(NO_3)_2{\cdot}6H_2O$ lose their weight gradually and finally steadied at ~30%, revealing the decomposition to corresponding oxides. PVP showed an intense weight loss at around 400 ºC and finally reached ~0 % before 600 ºC, indicating the complete decomposition to gas products. TEM, XRD, and Fourier transform infrared (FTIR) were further employed to check the products obtained at different calcination temperatures. As shown in **Figure 2g-j** and **Figure S23**, there are negligible morphology changes after 300 ºC calcination treatment, and corresponding XRD indicates the amorphous feature (**Figure 2k**). FTIR spectra shows an enhanced absorption band at 1500-1800 cm^{-1}, which can be indexed to the C=O stretching vibration, implying the partial oxidation of the PVP molecule (**Figure 2l**).[44] In comparison, small pores can be observed at the fibers after calcination at 400 ºC, and there are two weak diffraction peaks assigned to the La_2O_3 and $LaCoO_3$ in the XRD pattern. After calcination at 500 ºC, more obvious pores were formed and the diffraction peaks of $LaCoO_3$ can be clearly observed in the XRD pattern, indicating the further decomposition and gradual crystallization process. Meanwhile, the wide FTIR absorption bands in the range between 1300 and 1600 cm^{-1} were gradually weakened and finally disappear at 600 ºC, revealing the complete combustion of residual carbonaceous and nitrogenous species.[45] In addition, two strong absorption bands at 665 and 567 cm^{-1} can be observed at 400 ºC and disappeared at a higher temperature, while a new absorption band at around 586 cm^{-1} became stronger when the treated temperature raised gradually, suggesting the formation of Co_3O_4 and finally converted to perovskite during the treatment. **Figure 2m** summarizes the schematic illustration of the growth mechanism of the perovskite nanomesh. The metal precursors are evenly distributed in the original polymer fiber after electrospinning. During the calcination process, PVP molecules decompose into gaseous products (*e.g.*, CO_2, NO_x, and H_2O), while the metal nitrates also gradually decompose to corresponded metal oxides, which further migrate and finally crystallize to form the perovskite structure at high temperatures. Meanwhile, the forces caused by generous gas evolution can lead to a large number of pores and result in the highly porous nanomesh structure. It should be noted that too intense of such evolution is also unfavorable to maintain the 1D structure, where a suitable parameter (*e.g.*, metal precursors, concentrations, heat treatment conditions) is pivotal to result in the highly porous 1D perovskite nanomesh.

To understand the control mechanism behind the successful synthesis, the effects of various experimental parameters on the synthesis of LCO nanomesh were further carried out. As we mentioned before, the decomposition of metal nitrates and PVP to produce a large quantity of gaseous products is the primary process in forming the highly porous structure. As shown in **Figure S24**, nearly solid nanowires were obtained while using metal chlorides (*i.e.*, $LaCl_3{\cdot}6H_2O$ and $CoCl_2{\cdot}6H_2O$) as the metal precursors. This can be attributed to the difficult decomposition of metal chlorides, as confirmed by XRD (**Figure S24d**). Additionally, the concentration of metal precursor in the initial polymer solution is another important factor to generate 1D nanomesh structure. As shown in **Figure S25**, the fibers have broken into small particles when the concentration of metal precursor was too low, while the solid structure was obtained when the concentration is too excessive. During the calcination process, polymer molecules were completely decomposed into gas products and left out. Simultaneously, metal precursors were decomposed to corresponding oxides and retain in the result products. Consequently, if the metal species are too little to maintain the skeleton structure of pristine fibers, the 1D structure would destroy after the polymer was left out. On the other hand, too excessive concentration of metal precursor could cause a decreased polymer content, which reduces the forces caused by gas evolution and thus unfavorable for the formation of the porous structure. Therefore, a suitable concentration of the metal precursor was important to balance the formation of porosity and the maintaining of 1D structure. Additionally, a mild decomposition is important to obtain 1D nanomesh, where an over-fast heating rate would result in serious aggregation and fracture (**Figure S26**).

In general, the flexibility of ABO_3 perovskite structure could accommodate dopants of varied metals with different size and charge in A-site and B-site, thus effectively tailoring their catalytic properties via the electronic and local geometric structure regulation (e.g., orbital, spin, bond covalency, valence state, and atom coordination).[15,20,22] As a proof of concept, we demonstrated an A-site and B-site replacement strategy to optimize the OER performance of LCO substrate (**Figure 3a**). Benefited from the versatile synthesis methods, eight cobalt-based 1D perovskite nanomeshes, including LCO, $La_{0.5}Pr_{0.5}CoO_3$ (LPCO), $La_{0.5}Y_{0.5}CoO_3$ (LYCO), $La_{0.5}Ba_{0.5}CoO_3$ (LBCO), $LaCo_{0.8}Mn_{0.2}O_3$ (LCMO), $LaCo_{0.8}Fe_{0.2}O_3$ (LCFO), $LaCo_{0.8}Ni_{0.2}O_3$ (LCNO) and $La_{0.5}Ba_{0.5}Co_{0.8}Ni_{0.2}O_3$ (LBCNO) were studied. To evaluate the OER performance of various Co-based 1D perovskite nanomeshes, electrochemical measurements were performed with a standard three-electrode system. As shown in **Figure S27**, the introduction of Pr, Y and Ba demonstrated an obvious effect on the OER activity of pristine LCO nanomesh. Compared to LPCO nanomesh, LBCO nanomesh exhibits a more notable activity enhancement with a 55 mV reduction of overpotential at a current density of 20 mA cm^{-2}, while the LYCO shows degraded activity. Analogously, Ni presents the largest promotion among other transition metals during the substitution in B-sites, which delivers 1.9 times of current density to that of pristine LCO nanomesh at an overpotential of 370 mV (**Figure S28**). Accordingly, Ba and Ni were introduced simultaneously to expect a further improvement of OER activity. As summarized in **Figure 3b**, LBCNO nanomesh demonstrates the highest activity among other perovskite nanomeshes, which can deliver a current density of 92.3 mA cm^{-2} at potential of 1.6 V vs. RHE, and is about 7.4 times higher than that of LCO nanomesh, implying its optimal parameter towards OER. For further comparison, the OER performance of LCO particles prepared by the Pechini process (**Figure S29**) and commercial RuO_2 were also measured. **Figure 3c,d** show the polarization curves and corresponding Tafel plots of LBCNO nanomesh, LCO nanomesh, LCO particles and commercial RuO_2. Compared to the common

LCO particles, the 1D LCO nanomesh exhibits an obvious enhancement in terms of current density and Tafel slope. More excitingly, the optimized LBCNO nanomesh displays notable catalytic characteristics even better than that of benchmark RuO_2. Remarkably, LBCNO nanomesh requires the overpotential of only 287 mV and 339 mV for achieving a current density of 10 mA cm^{-2} and 50 mA cm^{-2}, respectively, much lower than that of RuO_2 (310 mV for 10 mA cm^{-2} and 382 mV for 50 mA cm^{-2}, respectively). Moreover, the Tafel slope for LBCNO nanomesh (61.3 mV dec^{-1}) is also smaller than that for RuO_2 (80.4 mV dec^{-1}), implying its faster OER kinetics. Furthermore, the Nyquist plot for LBCNO nanomesh exhibits a smaller interface charge-transfer resistance than that of the RuO_2 and other catalysts (**Figure 3e**), suggesting that the LBCNO nanomesh possesses a faster charge-transfer capacity during the OER process. Additionally, the mass activity (MA, normalized to the oxide mass loading) and specific activity (SA, normalized to the oxide surface area) of different catalysts were calculated for further comparison (**Figure S30**). As a result, both the MA and SA for 1D LBCNO nanomesh are significantly higher than those for other catalysts studied, indicating the indeed advantages of the simultaneous optimization of physical morphology and chemical composition (**Figure 3f** and **Figure S31**). Moreover, the OER performance of well-known $Ba_{0.5}Sr_{0.5}Co_{0.8}Fe_{0.2}O_{3-\delta}$ (BSCF) perovskite and NiFeOOH was measured under the same conditions for direct comparison (**Figures S32-S35**). Compared to the BSCF and NiFeOOH catalysts, the LBCNO nanomesh exhibits an obvious superiority in terms of current density and Tafel slope (**Figure S35**). Furthermore, the SA of LBCNO nanomesh is also higher than that of BSCF and NiFeOOH, indicating the excellent OER activity of LBCNO nanomesh. The durability of LBCNO nanomesh was then evaluated by chronopotentiometry (CP) measurement at a constant current density of 50 mA cm^{-2}. As shown in **Figure 3g**, the potential for LBCNO nanomesh remains almost unchanged during 30 h test, while considerable degeneracy was observed under the same testing conditions for commercial RuO_2. Further SEM, HRTEM, and EDS element analyses reveal that the morphology and structure of LBCNO nanomesh have largely maintained after OER. In addition, the continuous CV scans and XPS analyses of LBCNO nanomesh show negligible change, indicating the excellent stability of LBCNO nanomesh during OER (**Figures S36-S39**).

To gain insight into the origin of the intrinsic OER improvement of LBCNO nanomesh, the electronic and local geometric structure of LBCNO and LCO nanomeshes were studied by X-ray absorption spectroscopy (XAS). Firstly, we measured soft XAS spectra at the Co-$L_{2,3}$ edges in the total electron yield (TEY) mode. **Figure 4a** shows the Co L_3-edge XAS spectra of the LBCNO nanomesh, LCO nanomesh and several reference materials with different valence states of Co, including CoO (divalent), Sr_2CoRuO_6 (trivalent), and $SrCoO_3$ (tetravalent).[46,47] It is well known that Co $L_{2,3}$-edge is highly sensitive to Co ion's valence states, increasing in the Co valence state will cause a shift of the XAS spectrum toward higher energies. The edge peak shifts to higher energy from CoO to LBCNO, LCO, Sr_2CoRuO_6, and further $SrCoO_3$, suggesting the coexistence of Co^{2+} and Co^{3+} in LBCNO nanomesh and LCO nanomesh. To extract the detailed valence and the spin state information of Co ions in LBCNO nanomesh and LCO nanomesh, we simulated the experimental Co $L_{2,3}$-edge XAS spectral by superposing the spectra of relevant references: CoO for Co^{2+}, $EuCoO_3$ for Co^{3+} in the low spin (LS) state,[48] and Sr_2CoRuO_6 for Co^{3+} in the high spin (HS) state (**Figure 4b,c**).[46] As results, the average valence state of Co ions for LCO nanomesh was calculated to be +2.88 based on the fitted result of 12 % Co^{2+}, 38 % LS Co^{3+} and 50 % HS Co^{3+}. After the substitution with Ba and Ni, the average valence state of Co ions in LBCNO nanomesh decreases to +2.60, resulted from the decreased proportion of LS Co^{3+} and accompanying more occupation of Co^{2+}. The X-ray absorption near edge structure (XANES) analysis of Co *K*-edge spectra also verified the lower Co valence state of LBCNO nanomesh relative to LCO nanomesh (**Figure 4d**). Previously theoretical and experimental studies have shown that the high oxidation state Co (e.g., Co^{4+}) with enlarged Co-O bond covalency will weak the binding ability of metal cations with oxygen, which makes the direct O-O bonding more favorable, and thus lead to lattice oxygen mechanism (LOM).[49-52] The nonexistence of Co^{4+} in LBCNO and LCO nanomeshes implies the hard arousal of LOM. Additionally, both OER activities of LBCNO and LCO nanomeshes exhibit negligible pH dependence, which is in line with the concerted proton-electron transfer process, indicating the adsorbate evolution mechanism (AEM) dominated OER (**Figure S40**).[51] Furthermore, the local ligand environment of LBCNO and LCO nanomeshes were investigated by extended X-ray absorption fine structure (EXAFS) analysis at the Co *K*-edge XAS spectra. As shown in **Figure 4e** and **Figure S41**, the observed two main peaks in EXAFS spectra can be ascribed to the first and second coordination shell of the central Co atom comprising the six O atoms of the CoO_6 octahedron, and eight La/Ba atoms, respectively, as expected from perovskite structure. Further simulation reveals that the Co-O bond distances in LBCNO nanomesh (1.909 Å) is substantially short compared with LCO nanomesh (1.934 Å). Moreover, the intensity of the Co-O peak and fitted Co-O coordination number for LBCNO nanomesh are much lower than that of LCO nanomesh, suggesting the changed coordination geometry after incorporation, which can also be associated with the evolution of oxidation and spin states (**Table S2**). **Figure 4f** schematically depicts the electron configuration and charge-transfer models of Co ion. It has been reported that the OER reaction kinetics are primarily determined by the metal-oxygen binding. For instance, too weak of an oxygen binding results in the O* formation being the rate-limiting step, whereas too strong of an oxygen binding energy results in the O*-to- HOO* step becoming rate-limiting.[53] In perovskites, previous studies have shown that tuning the electronic configurations of transition metals by changing their oxidation states, orbital occupancy and coordination geometry, *etc.* will affect the covalency and hybridization of metal 3d and O 2p states, thus influence its adsorption with OER intermediates (i.e., HO*, O*, and HOO*).[18,54] In this regard, the regulated electronic configurations of LBCNO nanomesh are anticipated to meet the requirement of Sabatier's principle, which states that the interaction between the catalyst and the reaction intermediates should be neither too strong nor too weak.[55] Therefore, we conclude that the modifications of the spin state and oxidation state associated with the Co-O binding configuration in LBCNO nanomesh are responsible for the enhanced OER activity.

As demonstrated above, the ideal geometrical structure, as well as optimized intrinsic parameters, makes 1D LBCNO nanomesh a promising catalyst for practice electrochemical application. In order to demonstrate the applicability to water splitting, we constructed a two-electrode electrolyzer using carbon paper loaded with LBCNO nanomesh as the anode catalyst and commercial Pt/C (Johnson Matthey, 20 wt.% Pt on Vulcan carbon black) as the cathode catalyst (**Figure 4g** and **Figure S42**). As shown in **Figure 4h**, LBCNO (+) || Pt (−) electrode couple requires a cell voltage of only 1.57 V to achieve the water-splitting current density of 10 mA cm^{-2}, even lower than that for RuO_2 (+) || Pt (−) electrode couple (1.61 V). The electrolyzer with the LBCNO nanomesh anode also showed better durability than that with the RuO_2 anodes.

To unravel the significantly improved OER performances in the 1D perovskite nanomesh, the density functional theory (DFT) has been applied to investigate the electronic structures. For the pristine LCO, it is noted that the electronic distribution near the Fermi level (E_F) is dominated by the Co sites. The strong strain in the pristine LCO lattice limits the separation of electronic distribution (**Figure 5a**). With the introduction of Ni and Ba, the anti-bonding and bonding orbital distributions have been perturbed, where the electronic distribution of surface Co and La sites have become significantly enriched due to the release of the lattice strain by the doping, improving the electroactivity for OER. In addition, Ni sites also display highly electroactive, which further improves the interactions with O-species intermediates (**Figure 5b**). To further interpret the electronic structure of both LCO and LBCNO, we have plotted the projected partial density of states (PDOS). For the pristine LCO, the Co-3d orbitals display a splitting of 2.75 eV, which also crosses the E_F. The La-5d orbitals have occupied from E_V to E_V-4.0 eV (E_V = 0 eV), which only contributes to the stability of the structure due to the overlapping with both Co and O orbitals (**Figure 5c**). Meanwhile, the sharp Ni-3d orbitals are noted under the E_F, supporting the high electroactivity for electron transfer with adsorbates during OER. The splitting of Co-3d orbitals has been reduced to 2.25 eV after doping, indicating the slight change of the electronic environment of Co-sites, which is consistent with the experimental results. Moreover, the Ba-5p orbitals locate at a deep position at E_V-9.0 eV, which facilitates the stabilization of intermediates during OER owing to the p-p σ couplings (**Figure 5d**). The site-to-site PDOS of each element in LBCNO is also demonstrated. Notably, the La-5d orbitals show the relatively inert feature, which remains a similar electronic structure from the bulk to the surface. This indicates that La is playing an important role in stabilizing the lattice of doped LBCNO (**Figure 5e**). For the Ba doping, although the subtle difference of the dominant peak of Ba-5p is identified, the overall p-bands show a similar covering range from E_V-19.0 eV to E_V-9.0 eV, which are close to the O-2p bands in intermediates (**Figure 5f**). The site-to-site PDOS also confirms the change of Co-3d orbitals induced by the doping. The large 3d-splitting has been obviously alleviated from the bulk to the surface, which supports the improved electroactivity of Co sites (**Figure 5g**). For Ni-doping, the high position of Ni-3d orbitals is well preserved, in which the 3d orbitals become more concentrated at the surface. These results confirm the significant role of Ni in boosting up the OER performances in LBCNO through the enhanced electron transfer (**Figure 5h**). Within the s,p orbitals of the key intermediates, the σ orbitals offset of intermediates demonstrate the electron transfer process, which is affected by the interaction with the catalyst surface. The optimized electronic structure in LBCNO by doping has resulted in the relatively good linear correlation of the s,p orbitals in OER intermediates. Such a linear correlation lays a benign foundation to achieve efficient electron transfer during each reaction coordinate, which has successfully suppressed the overbinding and non-bonding of intermediates to guarantee a reduced overpotential for OER (**Figure 5i**).

Then, we have compared the reaction pathway of both LCO and LBCNO to demonstrate the energetic preference (**Figure 5j**). Under the equilibrium reaction environment (U = 0 V), the rate-determining step (RDS) occurs at the transformation of single adsorbed O* to HOO*, which shows an energy barrier of 1.62 and 1.75 eV, respectively. The conversion from HO* to O* is also much easier in LBCNO than in LCO (**Figure 5k**). With the applied standard potential of 1.23 V, the uphill reaction trend has been changed. Although the reaction trend for initial adsorption of HO* is more preferred in LCO, the large barrier in the reaction [O* + 2OH^- +H_2O] to [OOH + OH^- + H_2O] leads to the larger overpotential in OER. The overpotential has been estimated to be 0.39 eV and 0.53 eV, respectively, which is close to the experimental results in high current density (**Figure 5l**). Therefore, the improved performances of the doped 1D perovskite nanomesh LBCNO have been confirmed from both electronic and energetic perspectives.

Conclusion

In summary, we have reported a highly controllable modular strategy to fabricate 1D perovskite nanomeshes library by first employing facile electrospinning with the following calcination process, which is promising to realize the large-scalable production of well-defined nanostructures. Growth mechanism investigations indicate that the gaseous decomposition products of metal nitrates and polymer during calcination facilitate the formation of densely distributed pores, and a suitable precursor concentration is the key for generating high-quality 1D structure. As an exemplified application, the 1D perovskite nanomesh was applied towards the OER electrocatalysis. Benefit from the unique cross-linked and highly porous geometric features, abundant active sites and favorable reactants and electrical transport is enabled, which result in an apparent promotion to the OER electrocatalysis. The optimized 1D LBCNO nanomesh displayed a low overpotential of only 339 mV to achieve a current density of 50 mA cm^{-2}, and exhibited excellent stability during continuous electrolysis, already surpassing that of benchmark commercial RuO_2. DFT calculations have revealed that the additional Ni have demonstrated highly electroactive features and the Ba doping significantly enhances the stabilization of O-species. The optimized electronic structure by the metal doping has led to the improved performances of 1D perovskite nanomesh. Our work provides valuable guidance for improving the performance of perovskites through simultaneous morphology control and composition optimization and shows great potential for practice applications.

Acknowledgment

This work was financially supported by the Ministry of Science and Technology of China (2017YFA0208200, 2016YFA0204100), the National Natural Science Foundation of China (22025108, 21771156), the project of scientific and technologic infrastructure of Suzhou (SZS201708), the Priority Academic Program Development of Jiangsu Higher Education Institutions (PAPD), the start-up supports from Soochow University and the Early Career Scheme (ECS) fund (Grant No.: PolyU 253026/16P) from the Research Grant Council (RGC) in Hong Kong. The research in Dresden was partially supported by the DFG through SFB 1143. We acknowledge the support from the Max Planck-POSTECH-Hsinchu Center for Complex Phase Materials.

Declaration

The authors declare no competing financial interest.

References

(1) Chu, S.; Majumdar, A. Opportunities and challenges for a sustainable energy future. *Nature* **2012**, *488*, 294-303.

(2) Lewis, N. S. Research opportunities to advance solar energy utilization. *Science* **2016**, *351*, aad1920.

(3) Wang, X. X.; Swihart, M. T.; Wu, G. Achievements, challenges and perspectives on cathode catalysts in proton exchange membrane fuel cells for transportation. *Nat. Catal.* **2019**, *2*, 578-589.

(4) Jiao, Y.; Zheng, Y.; Jaroniec, M.; Qiao, S. Z. Design of electrocatalysts for oxygen- and hydrogen-involving energy conversion reactions. *Chem. Soc. Rev.* **2015**, *44*, 2060-2086.

(5) Seh, Z. W.; Kibsgaard, J.; Dickens, C. F.; Chorkendorff, I.; Nørskov, J. K.; Jaramillo, T. F. Combining theory and experiment in electrocatalysis: Insights into materials design. *Science* **2017**, *355*, eaad4998.

(6) Zhu, D. D.; Liu, J. L.; Qiao, S. Z. Recent advances in inorganic heterogeneous electrocatalysts for reduction of carbon dioxide. *Adv. Mater.* **2016**, *28*, 3423-3452.

(7) Li, Y.; Gong, M.; Liang, Y.; Feng, J.; Kim, J.-E.; Wang, H.; Hong, G.; Zhang, B.; Dai, H. Advanced zinc-air batteries based on high-performance hybrid electrocatalysts. *Nat. Commun.* **2013**, *4*, 1805.

(8) Bu, L.; Zhang, N.; Guo, S.; Zhang, X.; Li, J.; Yao, J.; Wu, T.; Lu, G.; Ma, J.-Y.; Su, D.; Huang, X. Biaxially strained PtPb/Pt core/shell nanoplate boosts oxygen reduction catalysis. *Science* **2016**, *354*, 1410-1414.

(9) Luo, M.; Zhao, Z.; Zhang, Y.; Sun, Y.; Xing, Y.; Lv, F.; Yang, Y.; Zhang, X.; Hwang, S.; Qin, Y.; Ma, J.-Y.; Lin, F.; Su, D.; Lu, G.; Guo, S. PdMo bimetallene for oxygen reduction catalysis. *Nature* **2019**, *574*, 81-85.

(10) Feng, Y.; Liu, H.; Yang, J. A selective electrocatalyst-based direct methanol fuel cell operated at high concentrations of methanol. *Sci. Adv.* **2017**, *3*, e1700580.

(11) Tiwari, J. N.; Sultan, S.; Myung, C. W.; Yoon, T.; Li, N.; Ha, M.; Harzandi, A. M.; Park, H. J.; Kim, D. Y.; Chandrasekaran, S. S.; Lee, W. G.; Vij, V.; Kang, H.; Shin, T. J.; Shin, H. S.; Lee, G.; Lee, Z.; Kim, K. S. Multicomponent electrocatalyst with ultralow Pt loading and high hydrogen evolution activity. *Nat. Energy* **2018**, *3*, 773-782.

(12) Shan, J.; Ling, T.; Davey, K.; Zheng, Y.; Qiao, S. Z. Transition-metal-doped RuIr bifunctional nanocrystals for overall water splitting in acidic environments. *Adv. Mater.* **2019**, *31*, 1900510.

(13) Seitz, L. C.; Dickens, C. F.; Nishio, K.; Hikita, Y.; Montoya, J.; Doyle, A.; Kirk, C.; Vojvodic, A.; Hwang, H. Y.; Norskov, J. K.; Jaramillo, T. F. A highly active and stable $IrO_x/SrIrO_3$ catalyst for the oxygen evolution reaction. *Science* **2016**, *353*, 1011-1014.

(14) Geng, Z.; Liu, Y.; Kong, X.; Li, P.; Li, K.; Liu, Z.; Du, J.; Shu, M.; Si, R.; Zeng, J. Achieving a record-high yield rate of 120.9 for N_2 electrochemical reduction over Ru single-atom catalysts. *Adv. Mater.* **2018**, *30*, 1803498.

(15) Hwang, J.; Rao, R. R.; Giordano, L.; Katayama, Y.; Yu, Y.; Shao-Horn, Y. Perovskites in catalysis and electrocatalysis. *Science* **2017**, *358*, 751-756.

(16) Yang, L.; Yu, G.; Ai, X.; Yan, W.; Duan, H.; Chen, W.; Li, X.; Wang, T.; Zhang, C.; Huang, X.; Chen, J.-S.; Zou, X. Efficient oxygen evolution electrocatalysis in acid by a perovskite with face-sharing IrO_6 octahedral dimers. *Nat. Commun.* **2018**, *9*, 5236.

(17) Calle-Vallejo, F.; Díaz-Morales, O. A.; Kolb, M. J.; Koper, M. T. M. Why is bulk thermochemistry a good descriptor for the electrocatalytic activity of transition metal oxides? *ACS Catal.* **2015**, *5*, 869-873.

(18) Suntivich, J.; May, K. J.; Gasteiger, H. A.; Goodenough, J. B.; Shao-Horn, Y. A perovskite oxide optimized for oxygen evolution catalysis from molecular orbital principles. *Science* **2011**, *334*, 1383-1385.

(19) Calle-Vallejo, F.; Inoglu, N. G.; Su, H.-Y.; Martínez, J. I.; Man, I. C.; Koper, M. T. M.; Kitchin, J. R.; Rossmeisl, J. Number of outer electrons as descriptor for adsorption processes on transition metals and their oxides. *Chem. Sci.* **2013**, *4*, 1245-1249.

(20) Guan, D.; Zhou, J.; Huang, Y.-C.; Dong, C.-L.; Wang, J.-Q.; Zhou, W.; Shao, Z. Screening highly active perovskites for hydrogen-evolving reaction via unifying ionic electronegativity descriptor. *Nat. Commun.* **2019**, *10*, 3755.

(21) Cheng, X.; Fabbri, E.; Yamashita, Y.; Castelli, I. E.; Kim, B.; Uchida, M.; Haumont, R.; Puente-Orench, I.; Schmidt, T. J. Oxygen evolution reaction on perovskites: A multieffect descriptor study combining experimental and theoretical methods. *ACS Catal.* **2018**, *8*, 9567-9578.

(22) Petrie, J. R.; Jeen, H.; Barron, S. C.; Meyer, T. L.; Lee, H. N. Enhancing perovskite electrocatalysis through strain tuning of the oxygen deficiency. *J. Am. Chem. Soc.* **2016**, *138*, 7252-7255.

(23) Chen, Y.; Li, H.; Wang, J.; Du, Y.; Xi, S.; Sun, Y.; Sherburne, M.; Ager, J. W.; Fisher, A. C.; Xu, Z. J. Exceptionally active iridium evolved from a pseudo-cubic perovskite for oxygen evolution in acid. *Nat. Commun.* **2019**, *10*, 572.

(24) Kim, B.-J.; Abbott, D. F.; Cheng, X.; Fabbri, E.; Nachtegaal, M.; Bozza, F.; Castelli, I. E.; Lebedev, D.; Schäublin, R.; Copéret, C.; Graule, T.; Marzari, N.; Schmidt, T. J. Unraveling thermodynamics, stability, and oxygen evolution activity of strontium ruthenium perovskite oxide. *ACS Catal.* **2017**, *7*, 3245-3256.

(25) Grimaud, A.; Demortière, A.; Saubanère, M.; Dachraoui, W.; Duchamp, M.; Doublet, M.-L.; Tarascon, J.-M. Activation of surface oxygen sites on an iridium-based model catalyst for the oxygen evolution reaction. *Nat. Energy* **2016**, *2*, 16189.

(26) Zhang, J.; Li, C. M. Nanoporous metals: fabrication strategies and advanced electrochemical applications in catalysis, sensing and energy systems. *Chem. Soc. Rev.* **2012**, *41*, 7016-7031.

(27) Xu, L.; Jiang, Q.; Xiao, Z.; Li, X.; Huo, J.; Wang, S.; Dai, L. Plasma-engraved Co_3O_4 nanosheets with oxygen vacancies and high surface area for the oxygen evolution reaction. *Angew. Chem. Int. Ed.* **2016**, *55*, 5277-5281.

(28) Pi, Y.; Shao, Q.; Wang, P.; Guo, J.; Huang, X. General formation of monodisperse IrM (M = Ni, Co, Fe) bimetallic nanoclusters as bifunctional electrocatalysts for acidic overall water splitting. *Adv. Funct. Mater.* **2017**, *27*, 1700886.

(29) Jiang, K.; Zhao, D.; Guo, S.; Zhang, X.; Zhu, X.; Guo, J.; Lu, G.; Huang, X. Efficient oxygen reduction catalysis by subnanometer Pt alloy nanowires. *Sci. Adv.* **2017**, *3*, e1601705.

(30) Ping, J.; Wang, Y.; Lu, Q.; Chen, B.; Chen, J.; Huang, Y.; Ma, Q.; Tan, C.; Yang, J.; Cao, X.; Wang, Z.; Wu, J.; Ying, Y.; Zhang, H. Self-assembly of single-layer CoAl-layered double hydroxide nanosheets on 3D graphene network used as highly efficient electrocatalyst for oxygen evolution reaction. *Adv. Mater.* **2016**, *28*, 7640.

(31) Bu, L.; Ding, J.; Guo, S.; Zhang, X.; Su, D.; Zhu, X.; Yao, J.; Guo, J.; Lu, G.; Huang, X. A general method for multimetallic platinum alloy nanowires as highly active and stable oxygen reduction catalysts. *Adv. Mater.* **2015**, *27*, 7204-7212.

(32) Bu, L.; Guo, S.; Zhang, X.; Shen, X.; Su, D.; Lu, G.; Zhu, X.; Yao, J.; Guo, J.; Huang, X. Surface engineering of hierarchical platinum-cobalt nanowires for efficient electrocatalysis. *Nat. Commun.* **2016**, *7*, 11850.

(33) Wu, Y.; Liu, X.; Han, D.; Song, X.; Shi, L.; Song, Y.; Niu, S.; Xie, Y.; Cai, J.; Wu, S.; Kang, J.; Zhou, J.; Chen, Z.; Zheng, X.; Xiao, X.; Wang, G. Electron density modulation of

$NiCo_2S_4$ nanowires by nitrogen incorporation for highly efficient hydrogen evolution catalysis. *Nat. Commun.* **2018**, *9*, 1425.

(34) Jiang, P.; Liu, Q.; Liang, Y.; Tian, J.; Asiri, A. M.; Sun, X. A cost-effective 3D hydrogen evolution cathode with high catalytic activity: FeP nanowire array as the active phase. *Angew. Chem. Int. Ed.* **2014**, *53*, 12855-12859.

(35) Ling, T.; Yan, D.-Y.; Jiao, Y.; Wang, H.; Zheng, Y.; Zheng, X.; Mao, J.; Du, X.-W.; Hu, Z.; Jaroniec, M.; Qiao, S. Z. Engineering surface atomic structure of single-crystal cobalt (II) oxide nanorods for superior electrocatalysis. *Nat. Commun.* **2016**, *7*, 12876.

(36) Zhao, B.; Zhang, L.; Zhen, D.; Yoo, S.; Ding, Y.; Chen, D.; Chen, Y.; Zhang, Q.; Doyle, B.; Xiong, X.; Liu, M. A tailored double perovskite nanofiber catalyst enables ultrafast oxygen evolution. *Nat. Commun.* **2017**, *8*, 14586.

(37) Taylor, G. I.; Dyke, M. D. V. Electrically driven jets. *Proc. R. Soc. Lond. A.* **1969**, *313*, 453-475.

(38) Lu, X.; Wang, C.; Wei, Y. One-dimensional composite nanomaterials: synthesis by electrospinning and their applications. *Small* **2009**, *5*, 2349-2370.

(39) Zhou, S.; Miao, X.; Zhao, X.; Ma, C.; Qiu, Y.; Hu, Z.; Zhao, J.; Shi, L.; Zeng, J. Engineering electrocatalytic activity in nanosized perovskite cobaltite through surface spin-state transition. *Nat. Commun.* **2016**, *7*, 11510.

(40) Hua, B.; Li, M.; Pang, W.; Tang, W.; Zhao, S.; Jin, Z.; Zeng, Y.; Shalchi Amirkhiz, B.; Luo, J.-L. Activating p-blocking centers in perovskite for efficient water splitting. *Chem* **2018**, *4*, 2902-2916.

(41) Zhu, Y.; Zhou, W.; Chen, Z.-G.; Chen, Y.; Su, C.; Tadé, M. O.; Shao, Z. $SrNb_{0.1}Co_{0.7}Fe_{0.2}O_{3-\delta}$ perovskite as a next-generation electrocatalyst for oxygen evolution in alkaline solution. *Angew. Chem. Int. Ed.* **2015**, *54*, 3897-3901.

(42) Hu, C.; Zhang, L.; Zhao, Z.-J.; Luo, J.; Shi, J.; Huang, Z.; Gong, J. Edge sites with unsaturated coordination on core-shell $Mn_3O_4@Mn_xCo_{3-x}O_4$ nanostructures for electrocatalytic water oxidation. *Adv. Mater.* **2017**, *29*, 1701820.

(43) Ge, J.; Wei, P.; Wu, G.; Liu, Y.; Yuan, T.; Li, Z.; Qu, Y.; Wu, Y.; Li, H.; Zhuang, Z.; Hong, X.; Li, Y. Ultrathin palladium nanomesh for electrocatalysis. *Angew. Chem. Int. Ed.* **2018**, *57*, 3435-3438.

(44) Loría-Bastarrachea, M. I.; Herrera-Kao, W.; Cauich-Rodríguez, J. V.; Cervantes-Uc, J. M.; Vázquez-Torres, H.; Ávila-Ortega, A. A TG/FTIR study on the thermal degradation of poly(vinyl pyrrolidone). *J. Therm. Anal. Calorim.* **2011**, *104*, 737-742.

(45) Chen, C.-Q.; Li, W.; Cao, C.-Y.; Song, W.-G. Enhanced catalytic activity of perovskite oxide nanofibers for combustion of methane in coal mine ventilation air. *J. Mater. Chem.* **2010**, *20*, 6968-6974.

(46) Chen, J.-M.; Chin, Y.-Y.; Valldor, M.; Hu, Z.; Lee, J.-M.; Haw, S.-C.; Hiraoka, N.; Ishii, H.; Pao, C.-W.; Tsuei, K.-D.; Lee, J.-F.; Lin, H.-J.; Jang, L.-Y.; Tanaka, A.; Chen, C.-T.; Tjeng, L. H. A complete high-to-low spin state transition of trivalent cobalt ion in octahedral symmetry in $SrCo_{0.5}Ru_{0.5}O_{3-\delta}$. *J. Am. Chem. Soc.* **2014**, *136*, 1514-1519.

(47) Potze, R. H.; Sawatzky, G. A.; Abbate, M. Possibility for an intermediate-spin ground state in the charge-transfer material $SrCoO_3$. *Phys. Rev. B* **1995**, *51*, 11501-11506.

(48) Hu, Z.; Wu, H.; Haverkort, M. W.; Hsieh, H. H.; Lin, H. J.; Lorenz, T.; Baier, J.; Reichl, A.; Bonn, I.; Felser, C.; Tanaka, A.; Chen, C. T.; Tjeng, L. H. Different look at the spin state of Co^{3+} ions in a CoO_5 pyramidal coordination. *Phys. Rev. Lett.* **2004**, *92*, 207402.

(49) Grimaud, A.; Diaz-Morales, O.; Han, B.; Hong, W. T.; Lee, Y.-L.; Giordano, L.; Stoerzinger, K. A.; Koper, M. T. M.; Shao-Horn, Y. Activating lattice oxygen redox reactions in metal oxides to catalyse oxygen evolution. *Nat. Chem.* **2017**, *9*, 457-465.

(50) Zhu, Y.; Tahini, H. A.; Hu, Z.; Chen, Z.-G.; Zhou, W.; Komarek, A. C.; Lin, Q.; Lin, H.-J.; Chen, C.-T.; Zhong, Y.; Fernández-Díaz, M. T.; Smith, S. C.; Wang, H.; Liu, M.; Shao, Z. Boosting oxygen evolution reaction by creating both metal ion and lattice-oxygen active sites in a complex oxide. *Adv. Mater.* **2020**, *32*, 1905025.

(51) Huang, Z.-F.; Song, J.; Du, Y.; Xi, S.; Dou, S.; Nsanzimana, J. M. V.; Wang, C.; Xu, Z. J.; Wang, X. Chemical and structural origin of lattice oxygen oxidation in Co-Zn oxyhydroxide oxygen evolution electrocatalysts. *Nat. Energy* **2019**, *4*, 329-338.

(52) Song, J.; Wei, C.; Huang, Z.-F.; Liu, C.; Zeng, L.; Wang, X.; Xu, Z. J. A review on fundamentals for designing oxygen evolution electrocatalysts. *Chem. Soc. Rev.* **2020**, *49*, 2196-2214.

(53) Man, I. C.; Su, H.-Y.; Calle-Vallejo, F.; Hansen, H. A.; Martínez, J. I.; Inoglu, N. G.; Kitchin, J.; Jaramillo, T. F.; Nørskov, J. K.; Rossmeisl, J. Universality in oxygen evolution electrocatalysis on oxide surfaces. *Chem. Cat. Chem.* **2011**, *3*, 1159-1165.

(54) Tong, Y.; Guo, Y.; Chen, P.; Liu, H.; Zhang, M.; Zhang, L.; Yan, W.; Chu, W.; Wu, C.; Xie, Y. Spin-state regulation of perovskite cobaltite to realize enhanced oxygen evolution activity. *Chem* **2017**, *3*, 812-821.

(55) Medford, A. J.; Vojvodic, A.; Hummelshøj, J. S.; Voss, J.; Abild-Pedersen, F.; Studt, F.; Bligaard, T.; Nilsson, A.; Nørskov, J. K. From the Sabatier principle to a predictive theory of transition-metal heterogeneous catalysis. *J. Catal.* **2015**, *328*, 36-42.

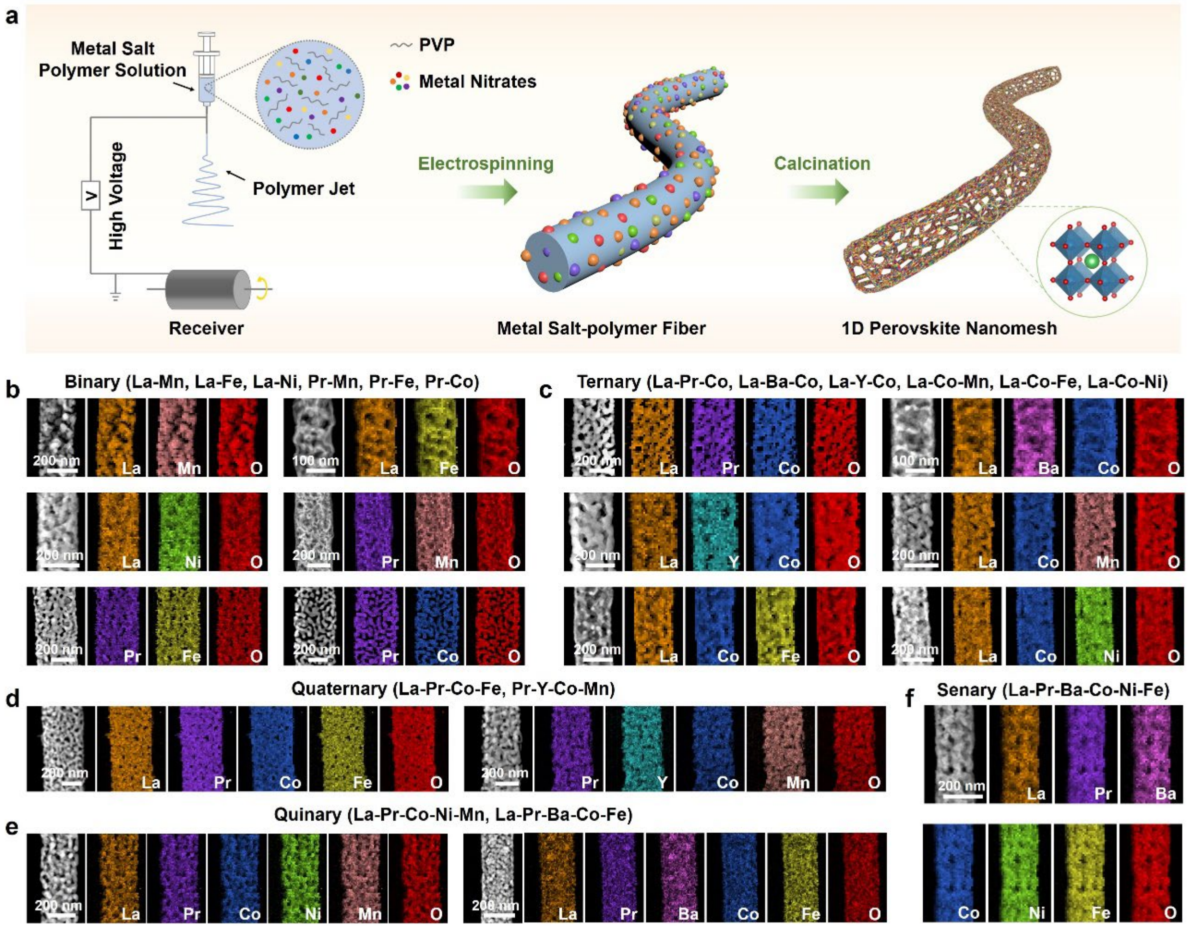

Figure 1. Synthetic scheme and characterization of 1D perovskite nanomeshes. (a) Schematic illustration for the synthetic process of 1D perovskite nanomeshes. HAADF-STEM images and corresponding elemental mappings of (b) binary (La-Mn, La-Fe, La-Ni, Pr-Mn, Pr-Fe, Pr-Co), (c) ternary (La-Pr-Co, La-Ba-Co, La-Y-Co, La-Co-Mn, La-Co-Fe, La-Co-Ni) 1D perovskite nanomeshes. (d) quaternary (La-Pr-Co-Fe, Pr-Y-Co-Mn), (e) quinary (La-Pr-Co-Ni-Mn, La-Pr-Ba-Co-Fe) and (f) senary (La-Pr-Ba-Co-Ni-Fe) 1D perovskite nanomeshes.

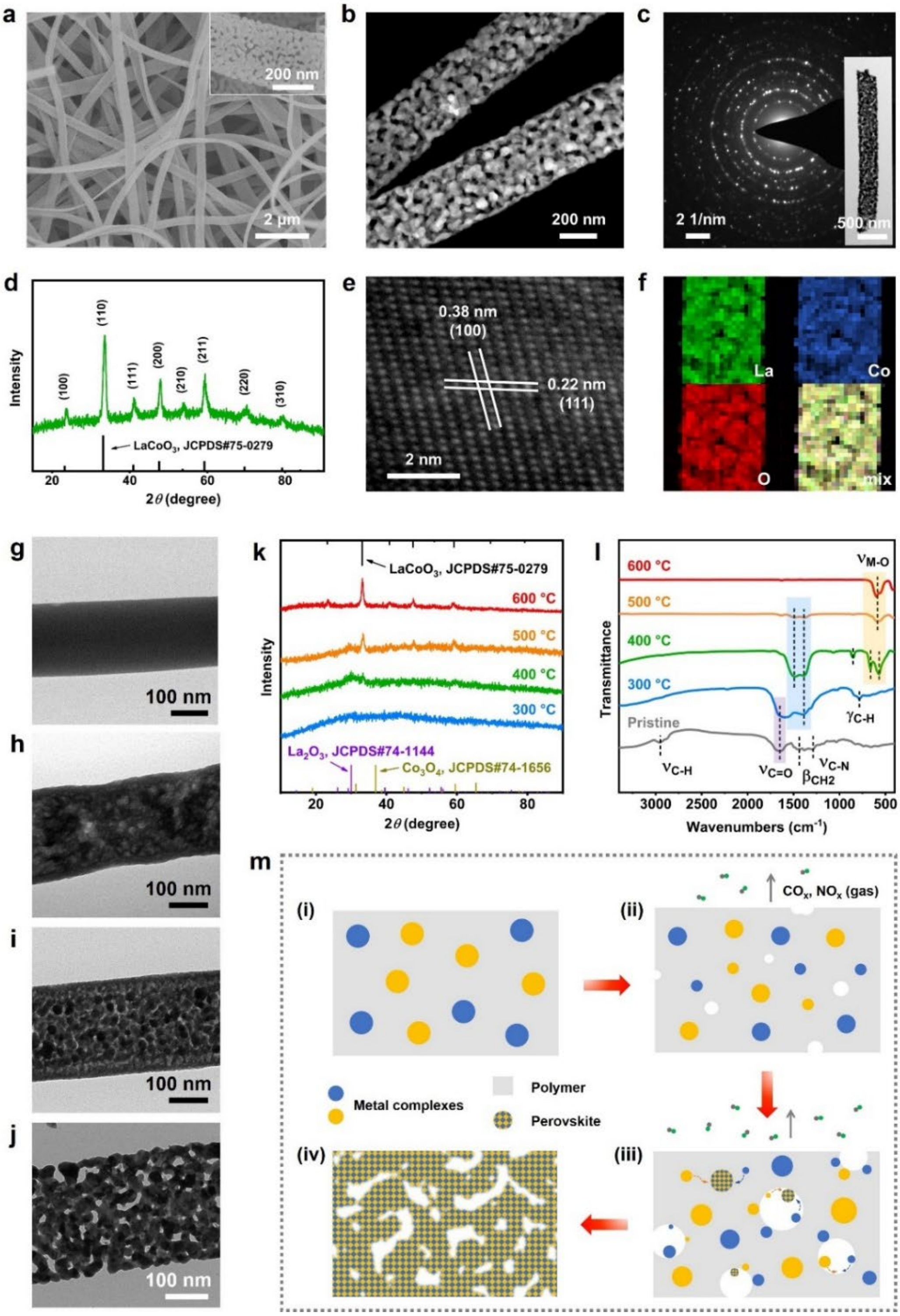

Figure 2. Growth mechanism for 1D LCO nanomeshes. (a) SEM images and (b) HAADF-STEM image of 1D LCO nanomeshes. (c) SAED pattern of an individual 1D LCO nanomesh, inset is the corresponding TEM image. (d) XRD pattern, (e) HRTEM image and (f) EDS elemental mapping of 1D LCO nanomeshes. TEM images of the products obtained at different calcination temperatures of (g) 300 ºC, (h) 400 ºC, (i) 500 ºC and (j) 600 ºC. (k) XRD patterns and (l) FTIR spectra of products obtained at different calcination temperatures. (m) Schematic illustration of the growth mechanism of the perovskite nanomeshes.

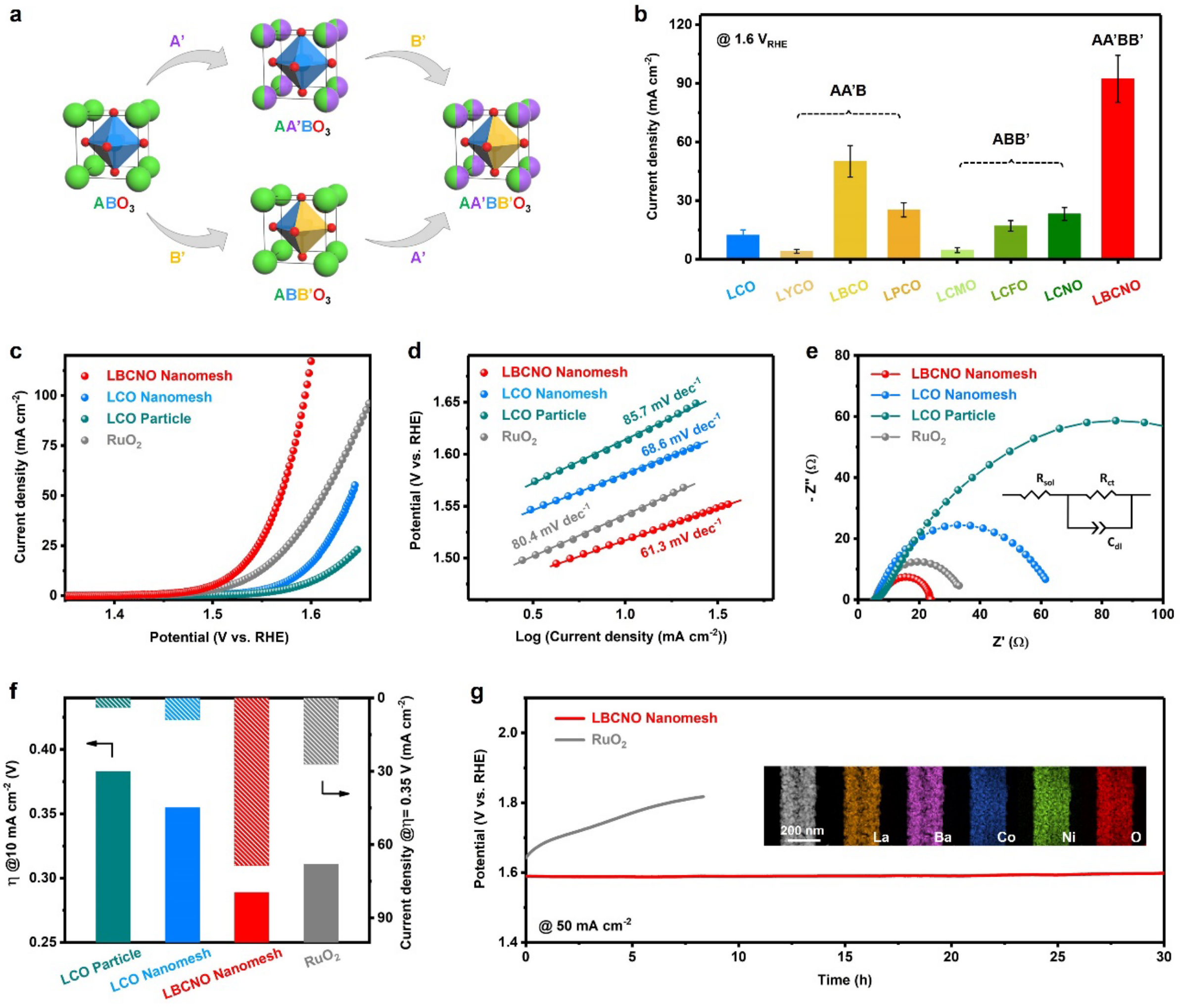

Figure 3. Electrochemical OER performance of 1D perovskite nanomeshes. (a) Doping strategies for perovskite ABO_3 (where A is an alkali or a rare earth metal, B is transition metal, and O is oxygen. (b) Current densities at 1.6 V vs. RHE of 1D perovskite nanomeshes with different compositions. (c) Polarization curves and (d) Tafel plots of 1D LBCNO nanomesh, 1D LCO nanomesh, LCO particle and commercial RuO_2. (e) Nyquist plots of the different catalysts at 1.55 V vs. RHE. The inset is the equivalent circuit model that contains the electrolyte resistance (R_{sol}), double layer capacitance (C_{dl}) and charge-transfer resistance (R_{ct}). (f) Overpotentials (η) at 10 mA cm^{-2} (left axis) and current densities at $\eta = 0.35$ V (right axis) of the different catalysts. (g) Chronopotentiometric (CP) curves of the 1D LBCNO nanomeshes and commercial RuO_2 at 50 mA cm^{-2}. Inset in (g) is the elemental mappings of 1D LBCNO nanomeshes after the CP test.

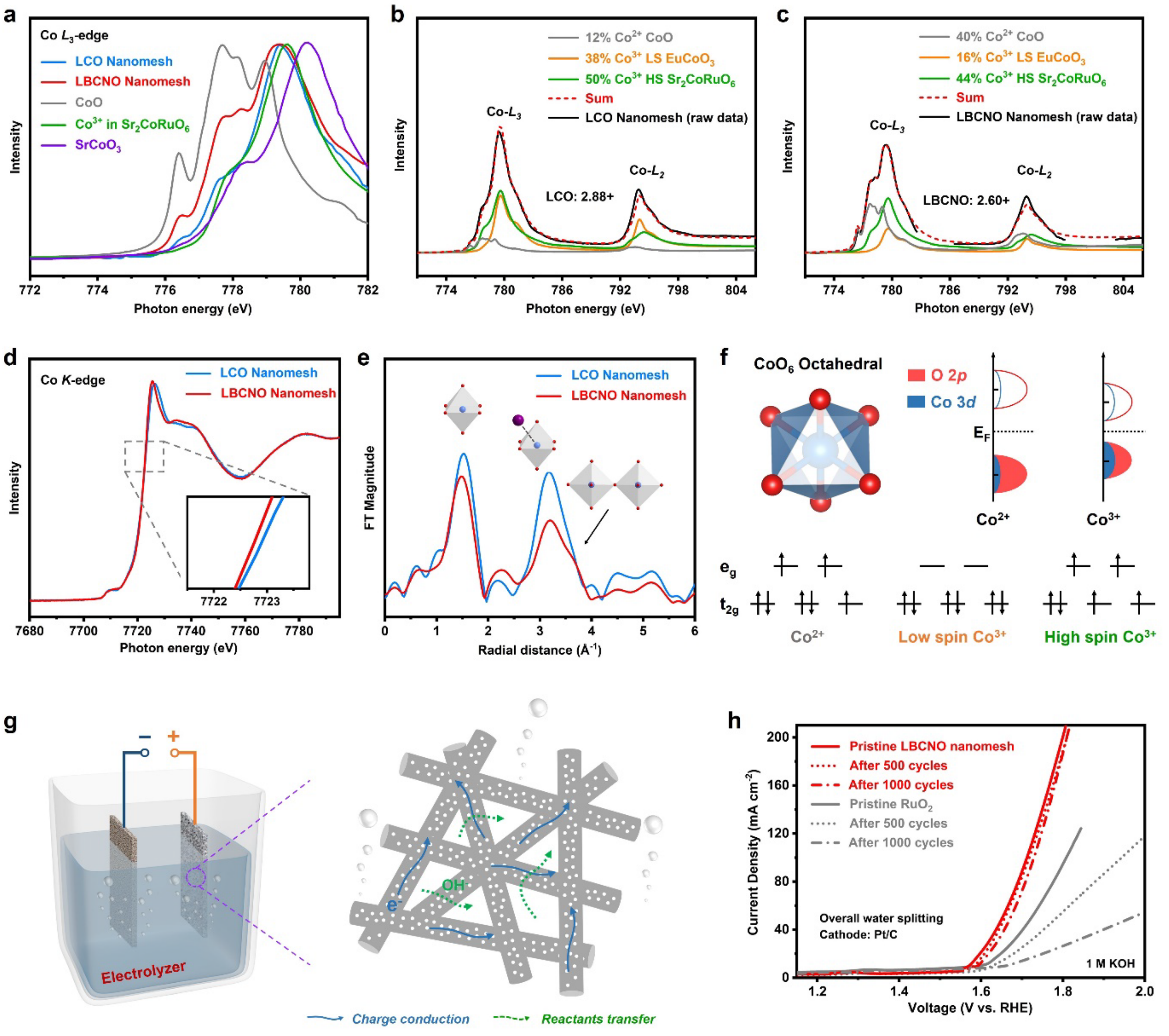

Figure 4. XAS analysis and overall water splitting experiments. (a) Co L_3-edge XAS spectra of the LCO and LBCNO nanomeshes, and several reference materials. Simulation of the Co $L_{2,3}$ XAS spectra of (b) LCO nanomesh and (c) LBCNO nanomesh by superposition of the spectral information from relevant reference materials. Data were collected using soft XAS with the total electron yield (TEY) mode. (d) Fourier transforms of EXAFS spectra collected at the Co *K*-edge and (e) XANES spectra of the LCO and LBCNO nanomeshes. Data were collected using hard XAS with transmission mode. (f) Schematic representations of the electronic structure and charge-transfer models for Co. (g) Schematic illustration of the overall water splitting setup and micro geometric structure of 1D perovskite nanomeshes. (h) Polarization curves of LBCNO nanomeshes and commercial RuO_2 for overall water splitting at pristine and after 500 cycles. Pt/C loaded on carbon paper was used as cathode.

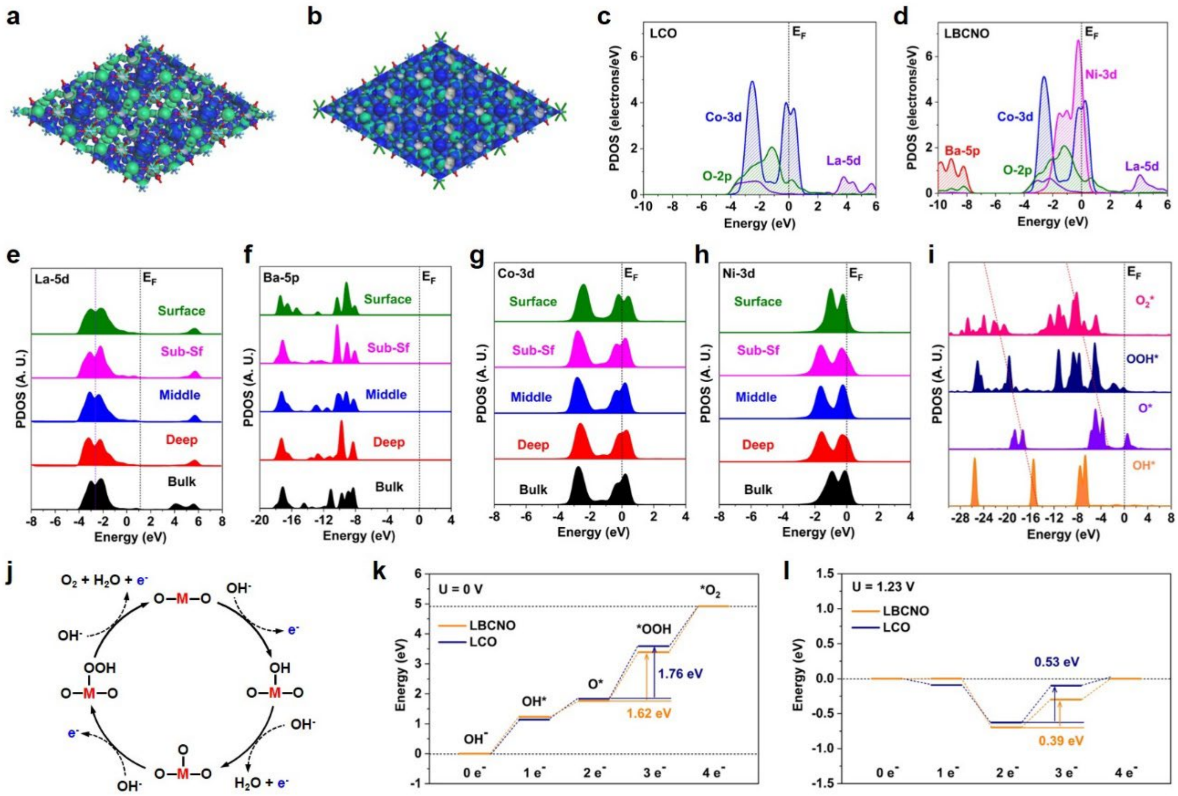

Figure 5. Theoretical calculations of 1D perovskite nanomeshes. (a) The real spatial 3D orbital contour plots for LCO. (b) The real spatial 3D orbital contour plots for LBCNO. (c) The PDOSs of LCO. (d) The PDOSs of LCBNO. The site-to-site PDOSs of (e) La-5d, (f) Ba-5p, (g) Co-3d and (h) Ni-3d in LBCNO. (i) The PDOS of *s,p* orbitals in O-species intermediates in OER. (j) OER reaction pathway on a metal ion site. The reaction trend comparison of OER under (k) U = 0 V and (l) U = 1.23 V.